Control of surface area and conductivity of niobium-added titanium oxides as durable supports for cathode of polymer electrolyte fuel cells

Yongbing Ma, Takaaki Nagai, Yuta Inoue, Kaoru Ikegami, Yoshiyuki Kuroda, Koichi Matsuzawa, Teko Napporn, Yan Liu, Shigenori Mitsushima, Akimitsu Ishihara

Materials and Design 203 (2021) 109623

Contents lists available at ScienceDirect

Materials and Design

journal homepage: www.elsevier.com/locate/matdes

Control of surface area and conductivity of niobium-added titanium oxides as durable supports for cathode of polymer electrolyte fuel cells

Yongbing Ma [a], Takaaki Nagai [b], Yuta Inoue [a], Kaoru Ikegami [b], Yoshiyuki Kuroda [a], Koichi Matsuzawa [c], Teko W. Napporn [b,d], Yan Liu [e], Shigenori Mitsushima [a,b], Akimitsu Ishihara [b,*]

[a] Graduate School of Engineering Science, Yokohama National University, Tokiwadai, Hodogaya-ku, Yokohama 240-8501, Japan
[b] Advanced Chemical Energy Research Center, Institute of Advanced Sciences, Yokohama National University, Tokiwadai, Hodogaya-ku, Yokohama 240-8501, Japan
[c] Graduate School of Engineering, Yokohama National University, Tokiwadai, Hodogaya-ku, Yokohama 240-8501, Japan
[d] IC2MP UMR 7285 CNRS University of Poitiers, 4 rue Michel Brunet B27 TSA 5110686073, Poitiers Cedex 09, France
[e] Beijing National Laboratory for Molecular Science, State Key Laboratory for Structural Chemistry of Unstable and Stable Species, College of Chemistry and Molecular Engineering, Academy for Advanced Interdisciplinary Studies, Peking University, Beijing 100871, China

HIGHLIGHTS

- Design of Nb-added TiO_2 as cathode supports for polymer electrolyte fuel cells.
- Control of specific surface area and conductivity of Nb-added TiO_2
- Specific surface area was strongly affected by the amount of Nb addition.
- Conductivity was governed by the ratio of Nb^{4+}.
- Superior durability of Nb-added TiO_2 in acidic and oxidative atmosphere.

GRAPHICAL ABSTRACT

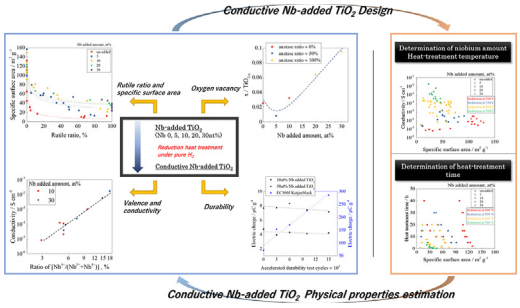

ARTICLE INFO

Article history:
Received 4 January 2021
Received in revised form 25 February 2021
Accepted 27 February 2021
Available online 2 March 2021

Keywords:
Conductive electrodes
Support cathode catalysts
Polymer electrolyte fuel cells
Carbon-free support

ABSTRACT

Niobium-added titanium oxide is a promising candidate as a substitute carbon support for cathodes of PEFCs. Nb-added TiO_2 can act as a support for platinum nanoparticles to enhance the oxygen reduction reaction (ORR) activity and durability under acidic conditions. Nb-added TiO_2 supports with the desired surface area (10–130 $m^2\ g^{-1}$) and conductivity (10^{-7}–10^{-2} S cm^{-1}) were prepared by changing the amount of Nb and the heat treatment conditions. First, we conducted a systematic investigation with changes in the amount of niobium addition, heat-treatment temperature, and time under a pure hydrogen atmosphere to reveal the physicochemical factors that govern the surface area and conductivity. Finally, we successfully proposed a procedure to prepare highly durable Nb-added TiO_2 supports with the desired surface area and conductivity by controlling the amount of niobium addition, heat-treatment temperature, and time under hydrogen. The charges of the double layer were almost unchanged after 5000 cycles of an accelerated durability test (ADT).

1. Introduction

Polymer electrolyte fuel cells (PEFCs) have attracted attention as electricity-generating devices with a high theoretical efficiency in terms of the energy conversion from hydrogen and oxygen into water [1]. PEFCs have already been applied to residential co-generation

* Corresponding author.
E-mail address: ishihara-akimitsu-nh@ynu.ac.jp (A. Ishihara).

https://doi.org/10.1016/j.matdes.2021.109623

systems, trains, and vehicles such as passenger cars, buses, and trucks. However, the actual efficiency of the present PEFCs is still low because of the large overpotential of the oxygen reduction reaction (ORR) at the cathode. The operation at higher voltages owing to an enhancement of the ORR activity, as well as at higher temperatures, is expected to improve the efficiency.

Although carbon is used as a catalyst support at the cathode in the present PEFCs owing to its high surface area, high electrical conductivity, and an appropriate morphology for the transfer of reactant oxygen gas and water product, carbon is easily oxidized because of the low standard electrode potential of carbon oxidation, i.e., 0.207 V, versus a reversible hydrogen electrode (RHE) [2,3]. In particular, the stability of carbon will become a serious problem at higher voltages and higher operating temperatures. As non-carbon electro-conductive materials, ceramics such as carbides and nitrides are existed. However, carbides and nitrides are easily dissolved to form oxides on the surface in an acidic and oxidative atmosphere. Therefore, electrically conductive oxides are promising candidates as stable supports under the cathode conditions of PEFCs [4–12]. Considering the cathode condition of PEFCs, because some oxides such as zinc-, manganese-, and cobalt-oxides easily dissolve in an acidic media, these are not appropriate as supports for PEFCs. Many studies on titanium-, tungsten-, tin-, cerium-, and molybdenum-oxide based materials as supports have been conducted to obtain higher durable ORR catalysts [4–9,12]. Among them, titanium- and tin-oxide based materials have been mainly investigated because of their high stabilities under acidic conditions [6,8,13–17]. For instance, in Ioroi et al.'s study [14], after 10,000 cycles of potential cycling between 1.0 and 1.5 V, the voltage losses for Pt-Ti/Ti_4O_7 MEA after 10,000 potential cycles are limited, and the Pt/XC72 MEA shows a severe performance degradation after ADT. In Jiménez-Morales et al.'s study [17], after 6000 ADT cycles from 1.0 to 1.6 V versus RHE in 0.1 M $HClO_4$, the mass activity of the 7Pt/1Ta/SnO_2 catalyst showed a 30% loss compared to a commercial Pt/C catalyst, which had 50% mass activity loss.

In this study, we focused on titanium-oxide based compounds as a support for cathode catalysts that enhance the ORR activity and durability [5,6,14,18–26]. Therefore, titanium-oxide based compounds are promising candidates as substitutes for carbon supports. It is believed that the first stage, indicating the availability of titanium-oxide based compounds as a support for Pt nanoparticles, has elapsed and the second stage for controlling properties such as the surface area and conductivity of titanium oxide-based compounds has arrived. In other words, the material design of the Nb-added TiO_2 is necessary for PEFC supports at present. Different properties are required according to the specific application. For example, in the case of a low loading of Pt particles, a high conductivity has precedent over a high surface area because the low loading of Pt cannot enhance the conductivity as a powder catalyst even if a high dispersion of Pt particles is easily achieved. By contrast, in the case of a high loading of Pt particles, the high surface area has precedent over a high conductivity because the high loading of Pt greatly enhances the conductivity as a powder catalyst, despite the difficulty of a high dispersion owing to an easy agglomeration.

Regarding the conductivity, the large bandgap of TiO_2 (approximately 3.2 eV and 3.0 eV for the anatase and rutile phases, respectively) leads to insufficient conductivity as a support. There are two ways to improve the conductivity of titanium-oxide based compounds. One way is the formation of Magnéli phases of titanium sub-oxides (Ti_nO_{2n-1}; $4 \leqq n \leqq 10$) [27,28], which have an excellent conductivity comparable to that of a carbon material. In particular, although metal suboxides are generally unstable in acidic and oxidative atmospheres, Ti_4O_7 shows both high conductivity and high stability under cathode conditions. However, a high temperature is generally required to prepare Ti_4O_7 and increase the particle size, which is not available as a support. Although low-temperature processes for synthesizing Ti_4O_7 have been investigated [29], it is difficult to obtain pure Ti_4O_7, resulting in an instability of the other suboxides as support.

The other way is the doping of foreign elements into TiO_2 to improve the conductivity through the formation of the doping level of electrons. Many elements, such as transition metals (Cu, Co, Ni, Cr, Mn, Mo, Nb, V, Fe, Ru, Au, Ag, and Pt) and non-metals (N, S, C, B, P, I, and F), have been investigated [30–33]. However, from the viewpoint of stability in an acidic environment, the doping elements are limited, and we have focused instead on niobium as the doping element. Group 5 oxides such as niobium- and tantalum-oxides are expected to be stable because these oxides are stable under cathode condition of PEFCs. In addition, the highest valence of Nb and Ta is different from titanium, resulting that the electronic state of TiO_2 matrix is strongly affected by doping. However, tantalum has small amount of resources and large atomic weight. In this study, niobium was chosen as doping element. Niobium-doped TiO_2 has been investigated as a transparent conductive thin film for many years [34–38]. It was previously shown that doped niobium ions improve the conductivity and inhibit the phase transformation from anatase to rutile, indicating that a decrease in the surface area owing to a heat treatment is restrained by the niobium doping. Therefore, niobium-doped TiO_2 powders have been applied as a support to an ORR catalyst [39–46]. Elezović et al. demonstrated that, although the electrochemical surface area (ECSA) of Pt-supported Nb-TiO_2 (42.5 $m^2 \cdot g^{-1}$ Pt) was smaller than that of Pt-supported carbon (96 $m^2 \cdot g^{-1}$ Pt), both the mass and specific activities at 0.9 V versus the RHE of Pt-supported Nb-TiO_2 (70 $mA \cdot mg^{-1}$ Pt and 0.165 $mA \cdot cm^{-2}$ Pt) were larger than those of Pt-supported carbon (73.8 $mA \cdot mg^{-1}$ Pt) [39]. He et al. also revealed that both the mass and specific activities at 0.9 V versus the RHE of Pt-supported Nb-TiO_2 prepared using an aerogel (150 mA mg^{-1} Pt and 349 μA cm^{-2} Pt) were larger than those of Pt-supported carbon (124 mA mg^{-1} Pt and 149 μA cm^{-2} Pt) [40]. In addition, Pt-supported carbon showed a 57.6% loss of ECSA over the course of the start-up/shut-down stability test (10,000 cycles) compared with Pt supported Nb-TiO_2 prepared using an aerogel, which lost only 22% of its initial ECSA, indicating its superior stability. Although other studies have also been conducted to show the applicability toward a highly durable support for ORR catalysts, the studies were conducted individually and not systematically.

Therefore, a systematic investigation of niobium-added titanium-oxide based compounds using parameters such as the amount of niobium addition, heat-treatment temperature, and heat-treatment time was attempted to conduct. A heat-treatment atmosphere was fixed with pure hydrogen to increase the oxygen vacancies according to previous studies [25,26,39,40,44,46]. In addition, Nb-added titanium oxide precursors were prepared using a hydrothermal method [47], and the specific surface area, conductivity, crystalline structure, and electronic state were evaluated. In this study, a scientific approach was applied to reveal the factors that affect the surface area and conductivity of Nb-added titanium oxide supports. An engineering approach was then used to prepare the desired surface area and conductivity of the supports. Finally, the electrochemical stability of a Nb-added titanium-oxide support was evaluated. We believe that both the scientific and engineering approach are necessary to develop the material design. In this study, the original approach was successfully performed to contribute the development of the Nb-added TiO_2 as durable support for PEFC cathodes.

2. Experimental

2.1. Preparation of Nb-added TiO_2 support

Nb-added TiO_2 precursors were prepared using the hydrothermal method reported by Lü et al. [47]. Titanium (IV) butoxide ($C_{16}H_{36}O_4Ti$, 97%, Sigma-Aldrich) and niobium (V) ethoxide ($C_{10}H_{25}NbO_5$, 99.95%, Sigma-Aldrich) were used as titanium and niobium sources, respectively. As an example, the preparation of 10 at.% Nb-added TiO_2 is described herein. First, 18 mmol of titanium (IV) butoxide and 2 mmol of niobium (V) ethoxide were mixed by stirring at room temperature,

30 mL of deionised water was dripped into the solution, and the solution was transferred into a 100 cm^3 Teflon-lined stainless autoclave for a hydrothermal reaction at 180 °C for 20 h. After cooling to room temperature, the precipitate was washed several times with deionised water and ethanol, and dried under vacuum at 80 °C for 12 h. To remove the remaining organics on the surface, 0.2 g of Nb-added TiO_2 was calcinated in air at 380 °C for 3 h to obtain the precursors. The amount of Nb added was controlled at 0, 5, 10, 20, and 30 at.% against Ti. Here, R_{Nb} is used to denote the ratio of added Nb. Heat treatment at a given temperature (500 °C, 550 °C, 600 °C, and 700 °C) for a given time under pure hydrogen was applied at a flow rate of 200 $cm^3\ min^{-1}$ to prepare the supports. The samples had some oxygen vacancies because of the heat treatment under H_2. Therefore, the exact chemical composition is expressed as $Nb_xTi_yO_z$. However, the samples with an at.% of Nb addition are donated as "at% Nb-added TiO_2" in this study. Herein, the term "added" was used instead of "doped" because in some cases niobium is segregated to form niobium oxide on the surface of the Nb-substituted TiO_2 particles.

2.2. Physico-chemical characterization

The crystalline structures of the Nb-added TiO_2 powders were analysed by X-ray diffraction (XRD; Rigaku Ultima IV) with Cu Kα radiation (λ = 0.15406 nm) in a scattering angle range of 10° to 90°. The Brunauer–Emmett–Teller (BET) specific surface areas of the synthesised supports were determined by nitrogen adsorption (BELSORP-mini, Microtrac BEL). The amount of oxygen vacancies was estimated using a thermal gravimetric (TG; Thermo plus EVO, Rigaku) analysis. The fundamental idea here is that the amount of oxygen vacancies can be estimated by the increase in weight of a sample during calcination in dry air. However, the amount of adsorbed water on the oxide surface must be excluded. Therefore, the weight of the adsorbed water per unit surface area by preparing a calibration curve using TiO_2 nanoparticles with different BET surface areas was estimated. The details are provided in Fig. S1(a)–(d). The apparent electrical conductivity of the support powders was measured under ambient air using a two-probe method. The powders were placed into a cylinder with a radius of 5.0 mm, and aluminium foil electrodes were placed at the top and bottom of the column of the powder. The electrical resistance was measured under an applied pressure of 60 MPa with a DC resistivity analyser (Resistance Meter, RM3545, Hioki). Fig. S2 shows the typical change in resistivity against the applied pressure for a high-conductive sample (30 at.% Nb-added TiO_2 heat-treated at 700 °C for 2 h under H_2) and (b) a low conductive sample (10 at.% Nb-added TiO_2 heat-treated at 550 °C for 20 h under H_2). The chemical states of the synthesised supports were investigated using X-ray photoelectron spectroscopy (XPS; PHI Quantum-2000, X-ray source: monochromated Al-Kα radiation). The peak of the C—C bond attributed to free carbon at 284.6 eV in the C 1 s spectrum was used to compensate for the surface charging. The surface morphology was observed using scanning electron microscopy (SEM, SU8000, Hitachi High-Technologies). The microstructures of the catalysts were analysed using transmission electron microscopy (TEM, JEOL LEM-2100F) and selected-area electron diffraction (SAED).

2.3. Electrochemical measurements

An oxide support (2 mg) was dispersed in a mixed solution of 300 mm^3 of hexanol (FUJIFILM Wako Pure Chemical, Ltd.) and 5 mm^3 of a 0.5-wt%Nafion® solution (Sigma-Aldrich) with ultrasonic treatment for 40 min to prepare the powder ink. Next, 10 mm^3 of powder ink was dropped onto a polished glassy carbon rod (GC; φ = 5.2 mm, Tokai Carbon Co., Ltd.) and dried at 60 °C for 1 h until the powder was supported with a loading of ~0.3 mg cm^{-2} to prepare a working electrode. For comparison, a powder ink containing 1 mg of carbon support (Ketjenblack EC-300 J; KB) was also dispersed in a mixed solution of 350 mm^3 of hexanol and 5 mm^3 of 0.5-wt%Nafion® solution, and ~ 0.13 mg cm^{-2} of KB was loaded onto the GC rod.

Electrochemical measurements were conducted using a 3-electrode cell in 0.1 M $HClO_4$ with a potentiostat (PS08, TOHO Technical Research). A glassy carbon plate and an RHE served as the counter and reference electrodes, respectively. An accelerated durability test (ADT) was conducted at a potential scan rate of 500 mV s^{-1} within the potential range from 1.0 to 1.5 V versus the RHE at 60 °C according to the start/stop cycle test recommended by the Fuel Cell Commercialization Conference of Japan (FCCJ) [48]. Cyclic voltammetry was carried out in 0.1 M $HClO_4$ under a pure N_2 flow at 60 °C with a scan rate of 50 $mV \cdot s^{-1}$ from 0.05 to 1.5 V versus the RHE to observe the electrochemical behaviour of the support surface during the ADT. The electric charge for the charge of the electrical double layer calculated from the anodic current within the potential range of 0.8 to 1.0 V versus the RHE was used to evaluate the stability of the supports.

3. Results and discussion

Fig. 1(a) and (b) show the XRD patterns of the Nb-added TiO_2 precursors with different amounts of added niobium. A Rigaku silicon (RSRP-43275G) standard powder was mixed with the precursors to calibrate the angular range. The crystalline structures of all precursors were identified as the anatase phase (JCPDS no. 00-021-1272). Fig. 1 (b) focuses on the shift of the anatase peak (101). As the amount of added niobium increased, the main peak of the anatase phase owing to (1 0 1) at 25.280° shifted to lower angles. This peak shift to lower angles was responsible for the lattice expansion of the anatase phase. Because the Shannon ionic radii of Nb^{5+} (64 pm) are slightly larger than that of Ti^{4+} (60.5 pm) for a coordination number of six [49], it is reasonable that substitution with Nb causes the peak to shift to lower angles. Thus, the peak shift to lower angles suggests that the amount of Nb ions substituted with Ti ions into the anatase phase increased as the amount of added Nb increased.

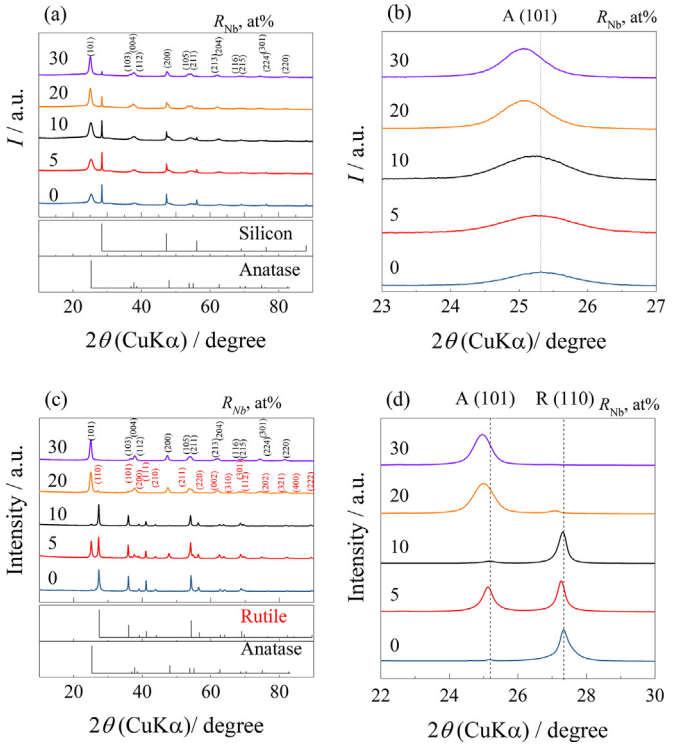

Fig. 1. (a) XRD patterns of Nb-added TiO_2 precursors with different amounts of added niobium and (b) peak shift of (1 0 1) of anatase. XRD patterns of Nb-added TiO_2 powders heat-treated at 600 °C for 5 h under pure hydrogen with different amounts of Nb addition with (c) a wide scan range of 10–90° and (d) a narrow range of 22–30°.

Heat treatment accelerates the phase transition from anatase to rutile. Fig. 1(c) and Fig. 1(d) show the XRD patterns of Nb-added TiO_2 powders heat-treated at 600 °C for 5 h under pure hydrogen with different amounts of Nb addition with (c) a scan range of 10–90° and (d) a narrow range of 22–30°. As shown in Fig. 1(c) and Fig. 1(d), both anatase and rutile peaks were observed in the 5 at.% Nb-added TiO_2. It is well known that the ratio of the rutile phase was proposed using XRD peaks to quantify the relative amounts of anatase and rutile in their mixtures [50]. The rutile (R_r) ratio was defined through the following equation [50]:

$$R_r = 1 - \left(1 + \frac{\frac{I_{rutile}}{0.79}}{I_{anatase}}\right)^{-1} \quad (1)$$

where I_{rutile} and $I_{anatase}$ were the intensities of the rutile (110) and anatase (1 0 1) peaks in the XRD pattern, respectively. For example, the R_r of the 5 at.% Nb-added TiO_2 heat-treated at 600 °C for 5 h under H_2 was calculated to be 50%.

Here, the previous experimental results regarding the effect of Nb-addition on the phase transition are summarized [51–57]. The doping of Nb^{5+}-substituted Ti^{4+} results in a decrease in the oxygen vacancies owing to the electroneutrality [53,57]. The oxygen vacancies accelerate the phase transition from anatase to rutile through an increase in the lattice relaxation [35,51,52,55]. Arbiol et al. reported that, in the case of a low amount of Nb addition in TiO_2 (up to 4 at.%), niobium was incorporated in TiO_2, thus decreasing the amount of oxygen vacancies, which inhibited the phase transformation [35]. By contrast, the ionic radii of Nb^{5+} (64 pm) are slightly larger than those of Ti^{4+} (60.5 pm) for a coordination number of six, indicating that the doping of Nb^{5+} inhibits the phase transition owing to the slight stress in the titania lattice [35,51,52,56,57]. In addition, in case of a large amount of Nb addition, the niobium oxides can be easily segregated on the titanium oxide particles to form strong Nb-O-Ti bands, resulting in an inhibited movement of surface Ti atoms required to initiate the phase transition [35,52,53]. Therefore, a large amount of Nb addition causes a phase transition to occur. These effects depend on the amount of Nb added.

Fig. 2 shows the dependence of R_r on the heat-treatment time of the Nb-added TiO_2 at (a) 500 °C, (b) 550 °C, (c) 600 °C, and (d) 700 °C. At 500 °C, little phase transformation occurred, as shown in Fig. 2(a).

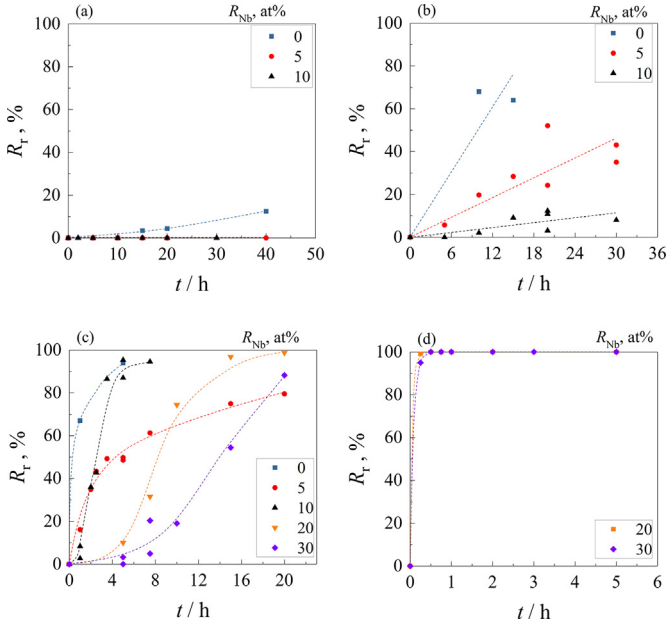

Fig. 2. Dependence of R_r on the heat-treatment time of the Nb-added TiO_2 at (a) 500 °C, (b) 550 °C, (c) 600 °C, and (d) 700 °C.

Only TiO_2 without Nb addition had slightly rutile peaks for a long heat treatment, such as over 15 h. When the heat-treatment temperature increased to 550 °C, the phase transformation proceeded almost linearly with respect to time, as shown in Fig. 2(b). In case of 5 at.% Nb-added TiO_2 showed large deviation for 20 h. However, as mentioned in Fig. 5 (b), the physico-properties such as the BET surface area and conductivity depend on the R_r. The phase transformation was inhibited as the amount of Nb added increased. When the heat-treatment temperature reached 600 °C, the tendency of the phase transformation was similar to that at 550 °C; that is, the phase transformation was restrained by the addition of Nb. However, 5 at.% Nb-added TiO_2 showed a different tendency, as shown in Fig. 2(c). In case of 5 at.% of Nb addition, the phase transition was delayed compared with that at 10 and 20 at.% of Nb addition. This behaviour will be discussed later in this section. At 700 °C, although 30 at.% Nb was added, the phase transformation could not be suppressed and a rutile state was not achieved after a short heat-treatment time, as shown in Fig. 2(d). Therefore, these results generally demonstrate the following: (1) The addition of Nb inhibited the phase transformation from anatase to rutile, that is, as the amount of Nb addition increased, the phase transformation was delayed. (2) The phase transformation accelerated with an increase in the heat-treatment temperature. These tendencies correspond with the previous results in the literature [51–57].

Here, the different behaviour of 5 at.% Nb-added TiO_2 at 600 °C is discussed according to Fig. 1(c), (d) and Fig. 2(c). As shown in Fig. 1 (c) and (d), the anatase phase still remained in the case of 5 at.% Nb-added TiO_2 heat-treated at 600 °C for 5 h, although the phase transformation almost completely proceeded for 10 at.% Nb-added TiO_2. In the case of 20 and 30 at.% Nb-added TiO_2, the anatase phase was almost completely stable. These results suggest that the anatase phase of the 5 at.% Nb-added TiO_2 was more stable than that of the 10 at.% Nb-added TiO_2 although the amount of Nb addition was low.

Before the discussion, it is necessary to recognise that the R_r of Nb-added TiO_2 powders heat-treated under H_2 is higher than those heat-treated under air. For example, the R_r of 5 at.% and 10 at.% Nb-added TiO_2 heat-treated at 600 °C for 5 h under H_2 were 50% and 85%, respectively, whereas the R_r of 4–10 at.% Nb-added TiO_2 heat-treated at the same temperature and time under air were less than 20% [52]. This difference was responsible for the formation of oxygen vacancies owing to the heat treatment under a reductive atmosphere of pure H_2. As mentioned above, the oxygen vacancies promote the phase transformation through an increase in lattice relaxation [35,51,52,55]. The oxygen vacancies were easily formed under reductive heat treatment compared with air at the same amount of Nb addition, heat-treatment temperature, and time, leading to a fast phase transformation under H_2. From this perspective, it was predicted that the structure of 5 at.% Nb-added TiO_2 heat-treated at 600 °C for 5 h under H_2 could change the rutile. However, as shown in Fig. 1(c) and (d), the anatase phase remained in the 5 at.% Nb-added TiO_2. When the amount of Nb added to TiO_2 was less than 4 at.%, niobium was incorporated into TiO_2 to decrease the number of oxygen vacancies, inhibiting the phase transformation [35]. Therefore, in the case of the 5 at.% Nb-added TiO_2, a small number of oxygen vacancies was formed even under a reductive heat-treatment to maintain the anatase phase. By contrast, a phase transformation almost completely occurred for 10 at.% Nb-added TiO_2. In the case of 10 at.% Nb, niobium was segregated from the TiO_2 lattice, which yielded an increase in the oxygen vacancies, and the phase transformation was no longer prevented [35], resulting in the R_r of the 10 at.% Nb-added TiO_2 reaching 95%. In the cases of 20 and 30 at.% Nb-added TiO_2, despite the possible formation of numerous oxygen vacancies, a large amount of niobium was segregated to form niobium oxides on the TiO_2 surface. The retardation of the anatase-to-rutile transformation by dispersed niobium oxides can be attributed to the formation of strong Nb-O-Ti bonds, which inhibit the movement of surface Ti atoms required to initiate the phase transformation [35,52,53], resulting in the anatase phase becoming stable, as shown in Fig. 2.

To confirm the above description, the amount of oxygen vacancies in the samples was quantified using TG-DTA. An estimation of the oxygen vacancies is shown in Fig. S1(a)–(d). Fig. 3 shows the relationship between the number of oxygen vacancies in the Nb-added TiO_2 heat-treated at 600 °C for 5 h under H_2 and the ratio of added Nb, R_{Nb}. As predicted, the oxygen vacancies decreased with an increase in R_{Nb} from 0 to 5 at.%. This was responsible for the Nb^{5+} incorporation into TiO_2 with electroneutrality. The oxygen vacancies increased almost linearly with an increase in R_{Nb} above 5 at.%. Therefore, the phase transformation was promoted as R_{Nb} increased above 5 at.%. In fact, the phase transition completely proceeded for 10 at.% Nb-added TiO_2. From the viewpoint of the amount of oxygen vacancies, the phase transformation accelerated above 10 at.%. However, as described above, the segregated niobium oxide inhibited the transition for 20 and 30 at.%.

The addition of niobium affects the growth of the rutile phase as well as the phase transition. The growth of the rutile phase influences the BET surface area, which is one of the important parameters used as a support. Fig. S3 shows FE-SEM images of the Nb-added TiO_2 heat-treated at 600 °C for 5 h under H_2 with (a) 0, (b) 5, (c) 10, (d) 20, and (e) 30 at.% of R_{Nb}. The BET surface areas of these samples were 12, 26, 30, 66, and 66 $m^2\ g^{-1}$, respectively. By contrast, the BET surface areas of the precursors with 0, 5, 10, 20, and 30 at.% of R_{Nb} were 132, 157, 150, 123, and 101 $m^2\ g^{-1}$, respectively. In addition, TiO_2 without Nb addition showed a drastic aggregation, as shown in Fig. S3(a), decreasing the BET surface area from 132 to 12 $m^2\ g^{-1}$. The 5 and 10 at.% Nb-added TiO_2 slightly aggregated to maintain the BET surface area at approximately 30 $m^2\ g^{-1}$. In the case of 10 at.% of R_{Nb}, the phase transition occurred almost completely, and only a rutile phase similar to TiO_2 without Nb addition was observed, as shown in Fig. 1(c). However, the aggregation of the rutile particles was entirely different, as shown in Figs. S2(a) and S2(c). This is due to the stress introduced by Nb-added in the TiO_2 lattice [21,35,57]. The slight difference in ionic radius between Nb^{5+} (64 pm) and Ti^{4+} (60.5 pm) hinders the growth of the rutile phase crystallites [55,56] as well as the phase transformation. Therefore, although the amount of oxygen vacancies in the TiO_2 without Nb addition and the 5 at.% Nb-added TiO_2 were almost the same, the aggregation of the rutile particles in the 5 at.% Nb-added TiO_2 was inhibited. In the case of 20 and 30 at.% Nb-added TiO_2, almost no aggregation was observed, and a relative high BET surface area, such as 66 and 65 $m^2\ g^{-1}$, was obtained.

Fig. 4 shows the TEM images of (a) 0, (c) 5, and (e) 10 at.% Nb-added TiO_2 and electron diffraction of (b) 0, (d) 5, and (f) 10 at.% Nb-added TiO_2 heat-treated at 600 °C for 5 h under H_2. As shown in Fig. 4(a), the TiO_2 without Nb addition had some small particles with a diameter of several nanometres on the surface of the large rutile particles. The small particles may be from a Magnéli phase such as Ti_4O_7 or Ti_3O_5 because the reduced titanium oxide was easily deposited on the surface [57]. The electron diffraction of the TiO_2 without Nb addition was not completely identified, but suggests the existence of Ti_3O_5 (Fig. S4 (a) and (b)). However, there were almost no small oxide particles on the surface of the 5 at.% Nb-added TiO_2, as shown in Fig. 4(c), revealing that Nb ions substituted the Ti ions in a relative manner, thereby decreasing the number of oxygen vacancies, as indicated in Fig. 3. This TEM image also supports the behaviour of the 5 at.% Nb-added TiO_2. In case of 10 at.% of R_{Nb}, some fine particles were also observed on the surface of the Nb-added TiO_2 particles with a diameter of several tens of nanometres, as shown in Fig. 4(e). Here, Ti_3O_5 and/or niobium oxides may segregate on the surface. However, electron diffraction, as shown in Fig. 4(f), was difficult to identify, and further observation is required to reveal the fine particles. From the ED pattern of the field of view, a large number of spots in a region with a relatively d value are extracted as shown in Fig. S4(a)- (f) with TEM images, and the d value is calculated, attribution of the closest chemical species compared to standard data (created from NIMS AtomWork) in Table S2.

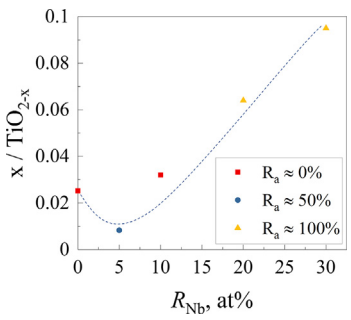

Fig. 3. Relationship between the number of oxygen vacancies of the Nb-added TiO_2 heat-treated at 600 °C for 5 h under H_2 and the ratio of added Nb, R_{Nb}.

Both the BET surface area and conductivity are important parameters for application to catalyst supports. Therefore, the BET surface area and conductivity are discussed as a function of the rutile ratio (R_r). As mentioned below, R_r becomes a suitable parameter for discussing the relation between the BET surface area, the conductivity, and the amount of Nb addition. Fig. 5 shows the dependence of the BET surface area and conductivity on R_r for samples with (a) 0, (b) 5, (c) 10, (d) 20, and (e) 30 at.% of R_{Nb}. As compared with the dependences of the BET surface area and the conductivity at different Nb additions, the dependences can be roughly divided into three patterns. First, in the case of TiO_2 without Nb addition, the BET surface area drastically decreased with a slight increase in R_r and over a wide range of R_r maintained a low value. By contrast, the conductivity of the precursor below 70% of R_r was low and drastically increased above approximately 70% of R_r. Second, in the case of 5 and 10 at.% R_{Nb}, the BET surface areas of the precursors were large and decreased exponentially with an increase in R_r. The conductivities of the precursors were low and remained almost constant below ~40% of R_r, and then gradually increased with an increase in R_r. In addition, although the 5 at.% Nb-added TiO_2 showed large deviation in Fig. 2(b) for 20 h treatment, Fig. 5(b) revealed that the BET surface area and conductivity depended on the R_r. The large deviation was probably responsible for the position of the added-Nb ions. The position of the Nb ions affected the BET surface area and conductivity through the R_r. Third, in the case of 20 and 30 at.% R_{Nb}, the BET surface areas largely decreased with an increase in R_r below approximately 10% and decreased slightly below 90%, and then drastically decreased again at above 90% of R_r. The conductivities showed almost a reverse dependence of the BET surface area, that is, the conductivities largely increased with an increase in R_r below approximately 10%, remained almost constant below 90%, and then drastically increased again above 90% of R_r. When R_r was used as a parameter, the effects of the acceleration and inhibition of the phase transition from anatase to rutile were excluded, and the characteristics of the anatase and rutile phases were reflected. Next, the dependences of the BET surface area and conductivity on R_r are discussed.

According to Fig. 5(a)–(e), the value of the BET surface area at a constant R_r can be obtained through an interpolation. Therefore, the dependence of the BET surface area on R_{Nb} at certain R_r values of 10%, 20%, 40%, and 60% are plotted in Fig. S5(a). The values of the precursors were also plotted. The BET surface area of the precursors was at maximum at 5 at.% of R_{Nb}. By contrast, the rate of the decrease in the BET surface area seemed to decrease with the increase in R_{Nb}. To clarify this, the ratio of the decrease in the BET surface area at a certain R_{Nb} was plotted against R_r, as shown in Fig. S5(b). In the case of TiO_2 without Nb addition, although the BET surface area of the precursor was relatively large, i.e., 132 $m^2\ g^{-1}$, it drastically decreased even at 10% of R_r because of the large particle growth of the rutile. In the case of the Nb addition, the ratios of the decrease in the BET surface area were not very large but decreased exponentially with an increase in R_r. The difference between without and with Nb addition was responsible for the stress introduced by Nb-doping in the TiO_2 lattice, and the effect increased with an increase in R_{Nb}. Therefore, the tendency of the BET surface area can be

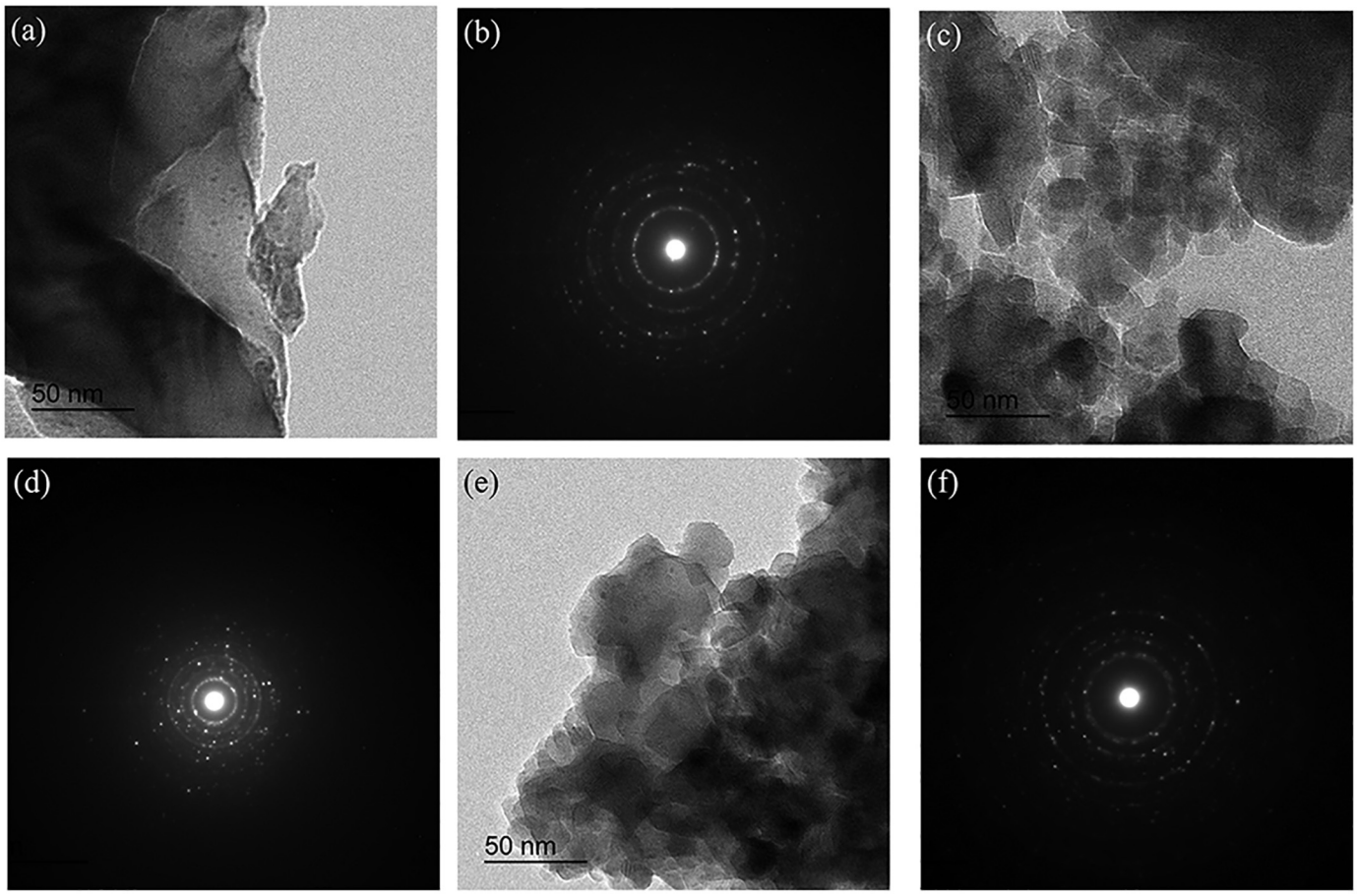

Fig. 4. TEM images of (a) 0, (c) 5, and (e) 10 at.% Nb-added TiO_2 and electron diffraction of (b) 0 (d) 5, and (f) 10 at.% Nb-added TiO_2 heat-treated at 600 °C for 5 h under H_2.

understood through R_r. For all added amounts, the relationship of R_r, conductivity and BET surface area are shown in Fig. S6(a) and (b).

To find suitable parameters that govern the conductivity, we focused on the electronic state of the samples. Fig. 6 shows the typical XPS of (a) Ti2p and (b) Nb3d of the 30 at.% Nb-added TiO_2 heat-treated at 700 °C for 15 min under H_2. Ti^{4+} and Nb^{5+} mainly existed, and lower valence states such as Ti^{3+} and Nb^{4+} were also observed in the sample. The XPS spectra of Ti2p and Nb3d of the other samples are shown in Fig. S7. For Ti 2p (Fig. 6(a)), the binding energies of 458.5 eV and 456.4 eV were TiO_2 and TiO_x [58], respectively; for Nb 3d (Fig. 6(b)), the binding energies of 206.8 eV and 204.8 eV were Nb_2O_5 and NbO_x [59], respectively. Peak separation was achieved, and the correlation between the ratio of Nb^{4+} or Ti^{3+} and the conductivity was investigated. In addition, because it is difficult to explain the dependence of the entire range of conductivity, we focused on the relatively high conductivity of above 10^{-5} S cm^{-1}. Fig. 6(c) shows the relationship between the logarithm of the ratio of Nb^{4+} and the logarithm of the conductivity above 10^{-5} S cm^{-1}, showing a good correlation between them. By contrast, the ratio of Ti^{3+} had no apparent correlation with the conductivity, as shown in Fig. S8. Fig. 6(c) roughly indicates that a twofold increase in the ratio of Nb^{4+} caused an order of magnitude greater conductivity of the samples. The reason is complicated because the conductivity was affected by the number of oxygen vacancies and the Nb addition, the electronic states of Nb and Ti, the particle size, and the contact resistance, among other factors. The contact resistance might be neglected in this high conductivity region because the conductivity was measured under a large pressurised condition of 60 MPa, as shown in Fig. S2. Nb-doped TiO_2 is essentially an n-type semiconductor, which is characterised by the carrier density and flat-band potential. Recently, the effect of semiconducting bulk properties of Nb-doped TiO_2 on the electrochemical behaviour under cathode conditions was investigated, demonstrating that the semiconducting properties govern the electrochemical active surface area owing to the formation of a depletion layer [60]. However, it is difficult to characterise the semiconducting properties of nanosized oxide particles because the particle size becomes smaller than the thickness of the space charge layer. In other words, a new approach based on the physical chemistry of nanosized oxide particles is required to discuss the electric conductivity of such fine-sized oxides [61]. In addition, if semiconducting properties such as the formation of a depletion layer affect the conductivity, the effect can be neglected because platinum nanoparticles are deposited on the oxide support for the application of cathode catalysts [62]. Therefore, in this study, the correlation between the conductivity and the ratio of Nb^{4+} was phenomenologically found and a further investigation will be applied to clarify the effect of Nb^{4+}.

On the other hand, the difference of the dependences of the conductivity and the BET surface area on the R_r as shown in Fig. S6(a) and (b) can be roughly explained. The dependences of the BET surface area on the R_r of all samples were essentially similar because the increase in the R_r indicated the longer heat-treatment time to cause the particle growth. On the other hand, the dependences of the conductivity of the samples can be divided into three patterns. In the case of TiO_2 without Nb addition, the rutile phase had also low conductivity because there was no Nb ions, resulting that the conductivity kept low below 70% of R_r. Above 70% of R_r, the rutile phase proceeded to transform into Magnéli phase to rapidly increase in the conductivity. In the case of 5 and 10 at.% of R_{Nb}, the conductivity gradually increased with increase in the R_r because the increase in the R_r produced the Nb^{4+} in

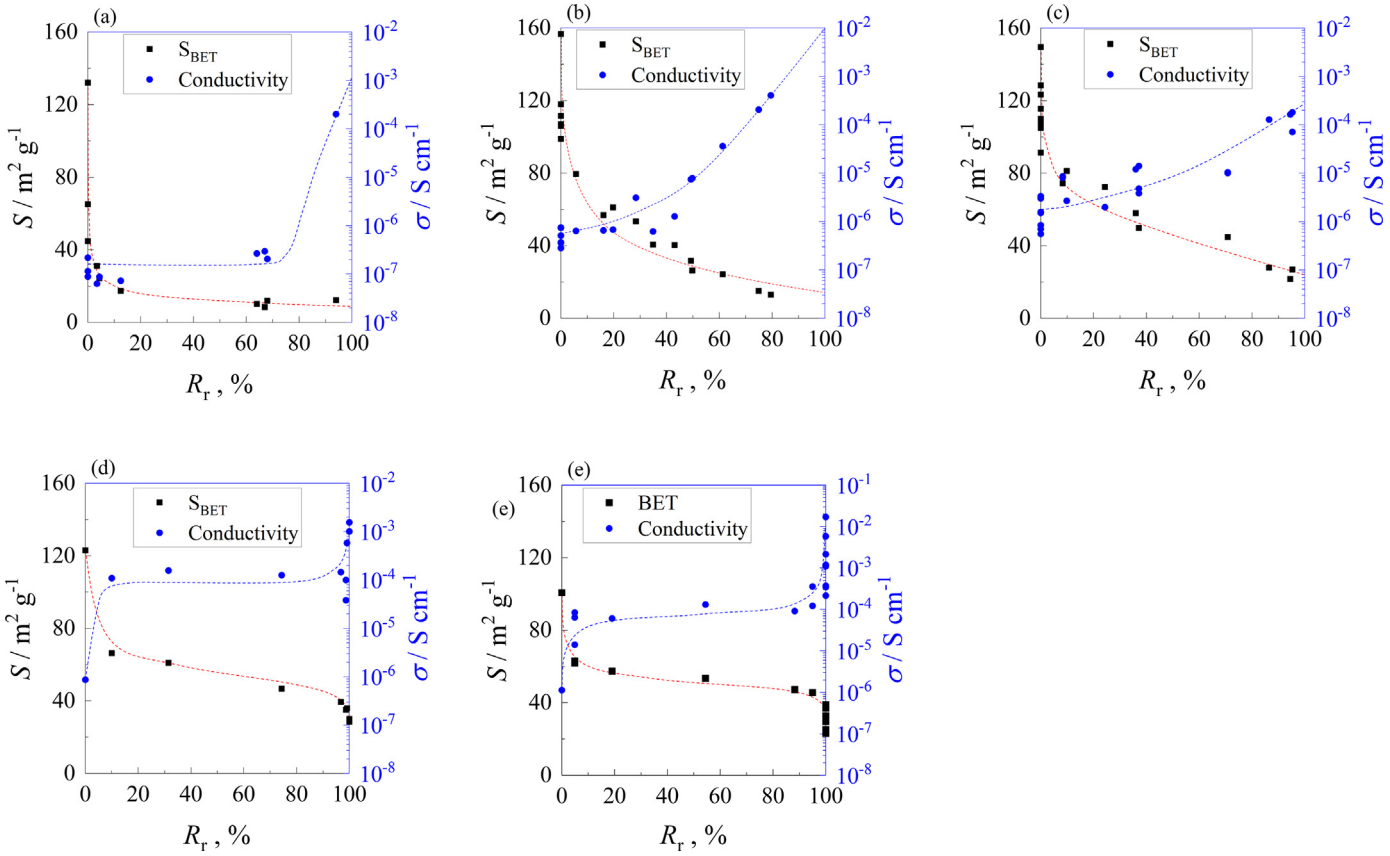

Fig. 5. Dependence of the BET surface area and conductivity on R_r for the samples with (a) 0, (b) 5, (c) 10, (d) 20, and (e) 30 at.% of R_{Nb}.

the samples. In the case of 20 and 30 at.% of R_{Nb}, Nb^{4+} was easy to produce even low R_r because the amount of added Nb was large. Above the R_r of 5%, the ratio of Nb^{4+} almost kept constant and the ratio of the Ti^{3+} increased with increase in the R_r. However, as shown in Fig. S8, the ratio of Ti^{3+} did not affect the conductivity.

A scientific approach was conducted, as described in the previous section. Next, an engineering approach will be useful to prepare Nb-added TiO_2 supports with different properties. The BET surface area and conductivity of the Nb-added TiO_2 as a support using three experimental parameters was attempted to control, namely, R_{Nb}, the heat-treatment temperature, and time. Fig. 7 (a) shows the relationship between the BET surface area and the logarithm of the conductivity of all samples heat-treated under H_2. The value of R_{Nb} and the heat-treatment temperature were distinguished based on the shape and colour of the plots, respectively. Roughly speaking, in the case of samples with a low R_{Nb}, such as 0, 5, or 10 at.% heat-treated at a lower temperature, a relatively large BET surface area was obtained instead of a low conductivity. However, in the case of samples with a large R_{Nb}, such as 20 or 30 at.%, a relatively high conductivity was obtained instead of a low BET surface area. Here, the procedure used to obtain the support with the desired BET surface area and the desired conductivity is described. The relationship between the heat-treatment time of all samples and the BET surface area for obtaining the heat-treatment time is shown in Fig. 7(b). First, the desired BET surface area and the desired conductivity are determined. For example, for the case I 125 $m^2\ g^{-1}$ of the BET surface area and 10^{-6} S cm^{-1} of the conductivity are desired.

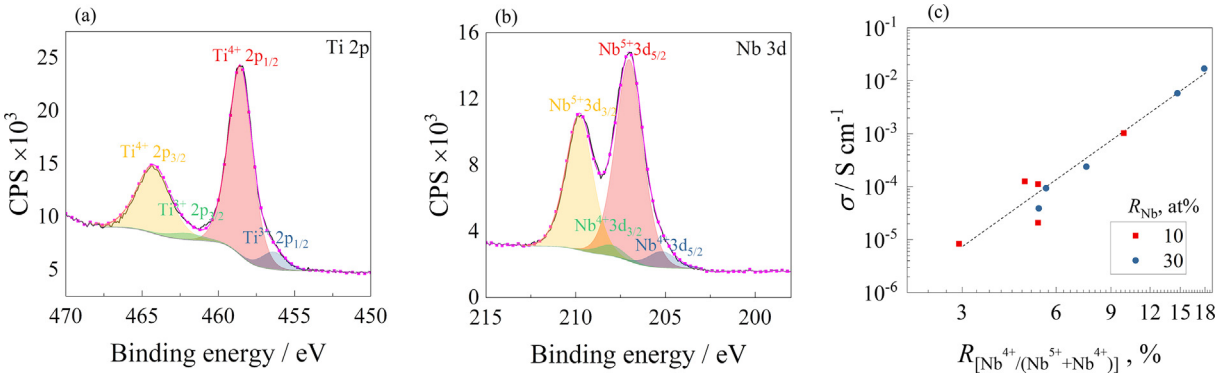

Fig. 6. Typical XPS of (a) Ti2p and (b) Nb3d of 30 at.% Nb-added TiO_2 heat-treated at 700 °C for 15 min under H_2. (c) Relationship between the logarithm of the ratio of Nb^{4+} and the logarithm of the conductivity above 10^{-5} S cm^{-1}.

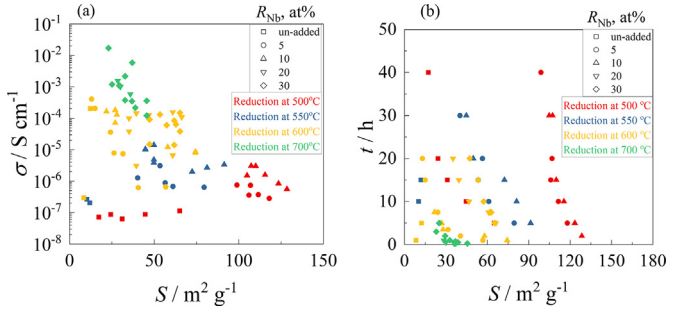

Fig. 7. (a) Relationship between the BET surface area and the logarithm of the conductivity of all samples heat-treated under H_2. (b) Relationship between the heat-treatment time of all samples and the BET surface area.

From the corresponding plot of 125 m^2 g^{-1} and 10^{-6} S cm^{-1}, we can read an R_{Nb} of 10 at.% and a heat-treatment temperature of 500 °C in the case of I. In addition, 10 at.% of R_{Nb} and a 500 °C heat-treatment temperature are obtained. Then, according to Fig. 7(b), the heat-treatment time can be obtained by reading the value of the y-axis of the plot of 10 at.% R_{Nb}, heat-treated at 500 °C, and a BET surface area of 125 m^2 g^{-1} along the x-axis. In the case of II, a BET surface area of 25 m^2 g^{-1} and a conductivity of 10^{-3} S cm^{-1} are desired. We can read an R_{Nb} of 30 at.% and a heat-treatment temperature of 700 °C. Then, according to Fig. 7(b), a 5-h heat-treatment time is obtained. Thus, the 30 at.% Nb-added TiO_2 will be heat-treated at 700 °C for 5 h, leading to a BET surface area of 25 m^2 g^{-1} and a conductivity of 10^{-3} S cm^{-1}. Based on Fig. 7(a) and (b), the BET surface area and conductivity of the Nb-added TiO_2 compounds could be controlled. This procedure is considerably useful for the preparation of supports with control of the BET surface area and conductivity.

Finally, the stability of the Nb-added TiO_2 heat-treated under H_2 was evaluated because some fine particles such as titanium suboxide or niobium oxides might be deposited on the surface of the Nb-added TiO_2. Many previous studies have previously revealed that platinum nanoparticles supported by Nb-added TiO_2 particles have superior stability under PEFC cathode conditions. Thus, the durability of the Nb-added TiO_2 supports based on two typical properties will be checked, i.e., a high BET surface area and low conductivity, and a low BET surface area and high conductivity. Two supports were prepared. For support 1, a high specific surface area of 128 m^2 g^{-1} and low conductivity of 5.57×10^{-7} S cm^{-1} are used (under preparation conditions of 10 at.% Nb-added TiO_2 heat-treated at 500 °C for 2 h under H_2). For support 2, a low specific surface area of 39 m^2 g^{-1} and a high conductivity of 2.15×10^{-4} S cm^{-1} are used (under preparation conditions of 30 at.% Nb-added TiO_2 heat-treated at 700 °C for 0.5 h under H_2). Ketjenblack (KB) EC-300 J, which is often used as a cathode catalyst support in PEFCs, was also evaluated to compare the stability.

The ADTs were conducted at a potential scan rate of 500 mV s^{-1} within the potential range of 1.0 to 1.5 V versus RHE at 60 °C according to the start/stop cycle test recommended by FCCJ [48]. Fig. 8 shows the cyclic voltammograms (CVs) during the ADT of (a) support 1, (b) support 2, and (c) KB EC-300 J in 0.1 M $HClO_4$ under N_2 at 60 °C with a scan rate of 50 mV·s^{-1}. Both supports 1 and 2 showed almost no change in CVs during ADT even after 15 k cycles, revealing that both supports with a high BET surface area and low conductivity, and a low BET surface area and high conductivity, were sufficiently stable as supports under the cathode conditions of PEFCs. By contrast, as shown in Fig. 8(c), the CV of Ketjenblack EC-300 J increased with an increasing number of cycles of ADT because of the surface oxidation owing to the potential cycling. Fig. 8(d) shows the variations in the electric charge for the charge of the double layer of supports 1 and 2, and KB EC300J under the number of cycles of ADT. Although some fluctuations

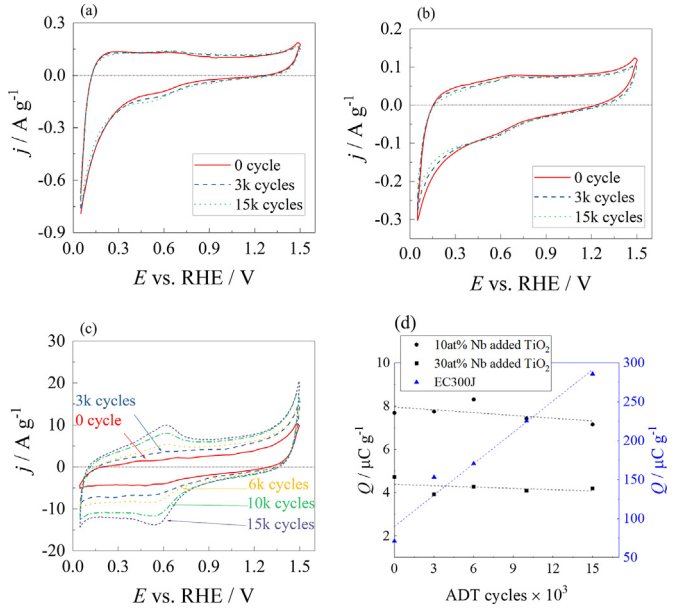

Fig. 8. Cyclic voltammograms (CVs) during the ADT of (a) support 1, (b) support 2, and (c) KB EC-300 J in 0.1 M $HClO_4$ under N_2 at 60 °C with a scan rate of 50 mV s^{-1}. (d) Variations in the electric charge of the double layer of supports 1 and 2, and KB EC300J in cycle numbers of ADT.

were observed, the capacitances of supports 1 and 2 were almost constant. Therefore, both typical supports showed a superior stability, indicating that the Nb-added TiO_2 as well as small particles such as titanium suboxides and/or niobium oxides had sufficient stability under cathode conditions. In the case of KB EC300J, the capacitance increased almost linearly with an increase in the number of cycles, suggesting that the surface of KB EC300J was oxidized through potential cycling within a high potential region.

Therefore, high-durable-Nb-added TiO_2 with the desired BET surface area and desired conductivity could be obtained by controlling the ratio of Nb addition, heat-treatment temperature, and time under H_2.

4. Conclusion

Material design of the Nb-added TiO_2 as catalyst supports for PEFC cathodes was proposed. Nb-added TiO_2 with the desired surface area and conductivity was synthesised. The physicochemical factors were aimed to reveal, that govern the surface area and conductivity through a systematic investigation with a change in the amount of niobium addition, heat-treatment temperature, and time. The behaviours such as a phase transition from anatase to rutile and the particle growth of the rutile phase can be explained through the previous findings in that the substituted Nb^{5+} decreased the number of oxygen vacancies. The oxygen vacancies promoted the phase transformation through an increase in lattice relaxation. The doped Nb inhibited both the transformation and growth of the rutile phase by the stress effect owing to the difference in the ionic radius, and the excess Nb segregated into niobium oxide on the surface of the Nb-added TiO_2 to restrict the phase transition. The BET surface area of the Nb-added TiO_2 was strongly affected by the amount of Nb addition, and the conductivity within the range of above 10^{-5} S cm^{-1} was governed by the ratio of Nb^{4+}. We then successfully proposed a procedure to prepare highly durable Nb-added TiO_2 supports with the desired BET surface area and conductivity by controlling the amount of niobium addition, heat-treatment temperature, and time under a pure hydrogen atmosphere.

CRediT authorship contribution statement

Yongbing Ma: Investigation. **Takaaki Nagai**: Investigation. **Yuta Inoue**: Investigation. **Kaoru Ikegami**: Investigation. **Yoshiyuki Kuroda**: Formal analysis. **Koichi Matsuzawa**: Investigation. **Teko W. Napporn**: Formal analysis. **Yan Liu**: Writing - original draft. **Shigenori Mitsushima**: Writing - original draft. **Akimitsu Ishihara**: Writing - review & editing.

Declaration of Competing Interest

The authors declare that they have no known competing financial interests or personal relationships that could have appeared to influence the work reported in this paper.

Acknowledgments

This research was supported by Strategic International Research Cooperative Program, Japan Science and Technology Agency (JST). The authors acknowledge financial support from the New Energy and Industrial Technology Development Organization (NEDO). This work was conducted under the auspices of the Ministry of Education, Culture, Sports, Science and Technology (MEXT) Program for Promoting the Reform of National Universities.

Appendix A. Supplementary data

Supplementary data to this article can be found online at https://doi.org/10.1016/j.matdes.2021.109623.

References

[1] P. Costamagna, S. Srinivasan, Quantum jump in the proton exchange membrane fuel cell science and technology from 1960 to the year 2000, part 2: engineering, technology development and applications aspect, J. Power Sources 102 (2001) 253–269, https://doi.org/10.1016/S0378-7753(01)00808-4.

[2] L. Roen, C. Paik, T. Jarvi, Electrocatalytic corrosion of carbon support in PEMFC cathodes, Electrochem. Solid-State Lett. 7 (2003) A19–A22, https://doi.org/10.1149/2F1.1630412.

[3] N. Macauley, D.D. Papadias, J. Fairweather, D. Spernjak, D. Langlois, R. Ahluwalia, K.L. More, R. Mukundan, R.L. Borup, Carbon corrosion in PEM fuel cells and the development of accelerated stress tests, J. Electrochem. Soc. 165 (2018) F3148–F3160, https://doi.org/10.1149/2F2.0061806jes.

[4] Z. Zhang, J. Liu, J. Gu, L. Sub, L. Cheng, An overview of metal oxide materials as electrocatalysts and supports for polymer electrolyte fuel cells, Energy Environ. Sci. 7 (2014) 2535–2558https://doi.org/10.1039/C3EE43886D.

[5] V. Elumalai, D. Sangeetha, Preparation of anion exchangeable titanate nanotubes and their effect on anion exchange membrane fuel cell, Mater. Des. 154 (2018) 63–72, https://doi.org/10.1016/j.matdes.2018.05.024.

[6] F. Ando, T. Tanabe, T. Gunji, T. Tsuda, S. Kaneko, T. Takeda, T. Ohsaka, F. Matsumoto, Improvement of ORR activity and durability of Pt electrocatalyst nanoparticles anchored on TiO_2/cup-stacked carbon nanotube in acidic aqueous media, Electrochim. Acta 232 (2017) 404–413, https://doi.org/10.1016/j.electacta.2017.03.004.

[7] I.A. Pašti, N.M. Gavrilov, S.V. Mentus, Electrocatalytic behavior of Pt/WO_3 composite layers formed potentiodynamically on tungsten surfaces, Int. J. Electrochem. Sci. 12 (2017) 5772–5791, https://doi.org/10.20964/2017.06.80.

[8] K. Kakinuma, M. Hayashi, T. Hashimoto, A. Iiyama, M. Uchida, Enhancement of the catalytic activity and load cycle durability of a PtCo alloy cathode catalyst supported on ta-doped SnO_2 with a unique fused aggregated network microstructure for polymer electrolyte fuel cells, ACS Appl. Energy Mater. 3 (2020) 6922–6928, https://doi.org/10.1021/acsaem.0c00993.

[9] F. Xu, D. Wang, B. Sa, Y. Yu, S. Mu, One-pot synthesis of Pt/CeO_2/C catalyst for improving the ORR activity and durability of PEMFC, Int. J. Hydrog. Energy 42 (2017) 13011–13019, https://doi.org/10.1016/j.ijhydene.2017.04.039.

[10] J. Wang, B. Wang, Z. Wang, L. Chen, C. Gao, B. Xu, Z. Jia, G. Wu, Synthesis of 3D flower-like ZnO/$ZnCo_2O_4$ composites with the heterogeneous interface for excellent electromagnetic wave absorption properties, J. Colloid Interface Sci. 586 (2021) 479–490, https://doi.org/10.1016/j.jcis.2020.10.111.

[11] Z. Gao, Z. Jia, K. Wang, X. Liu, L. Bi, G. Wu, Simultaneous enhancement of recoverable energy density and efficiency of lead-free relaxor-ferroelectric BNT-based ceramics, Chem. Eng. J. 402 (2020) 125951, https://doi.org/10.1016/j.cej.2020.125951.

[12] P.F.B.D. Martin, E.A. Ticianelli, Electrocatalytic activity and stability of platinum nanoparticles supported on carbon–molybdenum oxides for the oxygen reduction reaction, ChemElectroChem 2 (2015) 1298–1306, https://doi.org/10.1002/celc.201500196.

[13] X. Cao, F. Li, R. Yang, Non-carbon support materials used in low-temperature fuel cells, nanostructured materials for next-generation energy storage and conversion, Springer (2018) 145–170, https://doi.org/10.1007/978-3-662-56364-9_5.

[14] T. Ioroi, Z. Siroma, S. Yamazaki, K. Yasuda, Electrocatalysts for PEM fuel cells, Adv. Energy Mater. 9 (2019) 1801284, https://doi.org/10.1002/aenm.201801284.

[15] E. Fabbri, A. Rabis, Y. Chino, M. Uchida, T.J. Schmidt, Boosting Pt oxygen reduction reaction activity by tuning the tin oxide support, Electrochem. Commun. 83 (2017) 90–95, https://doi.org/10.1016/j.elecom.2017.09.006.

[16] G. Cognard, G. Ozouf, C. Beauger, L. Dubau, M. López-Haro, M. Chatenet, F. Maillard, Insights into the stability of Pt nanoparticles supported on antimony-doped tin oxide in different potential ranges, Electrochim. Acta 245 (2017) 993–1004, https://doi.org/10.1016/j.electacta.2017.05.178.

[17] I. Jiménez-Morales, F. Haidar, S. Cavaliere, D. Jones, J. Rozière, Strong interaction between platinum nanoparticles and tantalum-doped tin oxide nanofibers and its activation and stabilization effects for oxygen reduction reaction, ACS Catal. 10 (2020) 10399–10411, https://doi.org/10.1021/acscatal.0c02220.

[18] T. Tonosako, Z. Noda, J. Matsuda, M. Nishihara, A. Hayashi, K. Sasaki, Pt-TiO_2 nanocomposite PEFC electrocatalysts for high potential cycle durability, ECS Trans. 98 (2020) 523, https://doi.org/10.1149/09809.0523ecst.

[19] C. Yao, F. Li, X. Li, D. Xia, Fiber-like nanostructured Ti_4O_7 used as durable fuel cell catalyst support in oxygen reduction catalysis, J. Mater. Chem. 22 (2012) 16560–16565, https://doi.org/10.1039/C2JM32866F.

[20] Y. Kuroda, H. Igarashi, T. Nagai, T.W. Napporn, K. Matsuzawa, S. Mitsushima, K. Ota, A. Ishihara, Templated synthesis of carbon-free mesoporous Magnéli-phase titanium suboxide, Electrocatalysis 10 (2019) 459–465, https://doi.org/10.1007/s12678-019-00544-3.

[21] E.C.M. Barbosa, L.S. Parreira, I.C. de Freitas, L.R. Aveiro, D.C. de Oliveira, M.C. dos Santos, P.H.C. Camargo, Pt-decorated TiO_2 materials supported on carbon: increasing activities and stabilities toward the ORR by tuning the Pt loading, ACS Appl. Energy Mater. 2 (2019) 5759–5768, https://doi.org/10.1021/acsaem.9b00879.

[22] K.M. Naik, E. Higuchi, H. Inoue, Two-dimensional oxygen-deficient TiO_2 nanosheets-supported Pt nanoparticles as durable catalyst for oxygen reduction reaction in proton exchange membrane fuel cells, J. Power Sources 455 (2020) 227972, https://doi.org/10.1016/j.jpowsour.2020.227972.

[23] S. Bukka, R. Badam, R. Vedarajan, N. Matsumi, Photo-generation of ultra-small Pt nanoparticles on carbon-titanium dioxide nanotube composites: a novel strategy for efficient ORR activity with low Pt content, Int. J. Hydrog. Energy 44 (2019) 4745–4753, https://doi.org/10.1016/j.ijhydene.2019.01.004.

[24] A. Lewera, L. Timperman, A. Roguska, N. Alonso-Vante, Metal-Support Interactions between nanosized Pt and metal oxides (WO_3 and TiO_2) studied using X-ray photoelectron spectroscopy, J. Phys. Chem. C 115 (2011) 20153–20159, https://doi.org/10.1021/jp2068446.

[25] B.-J. Hsieha, M.-C. Tsaia, C.-J. Pana, W.-N. Sub, J. Ricka, H.-L. Choub, J. Fu Leec, B.-J. Hwang, Tuning metal support interactions enhances the activity and durability of TiO_2-supported Pt nanocatalysts, Electrochim. Acta 224 (2017) 452–459, https://doi.org/10.1016/j.electacta.2016.12.020.

[26] A. Bauer, K. Lee, C. Song, Y. Xie, J. Zhang, R. Hui, Pt nanoparticles deposited on TiO_2 based nanofibers: electrochemical stability and oxygen reduction activity, J. Power Sources 195 (2010) 3105–3110, https://doi.org/10.1016/j.jpowsour.2009.11.107.

[27] S. Andersson, B. Collén, U. Kuylenstierna, A. Magnéli, Phase analysis studies on the titanium-oxygen system, Acta Chem. Scand. 11 (1957) 1641–1652, https://doi.org/10.3891/acta.chem.scand.11-1641.

[28] J. Smith, F. Walsh, R. Clarke, Electrodes based on Magnéli phase titanium oxides: the properties and applications of Ebonex® materials, J. Appl. Electrochem. 28 (1998) 1021–1033, https://doi.org/10.1023/A:1003469427858.

[29] S. Tominaka, Y. Tsujimoto, Y. Matsushita, K. Yamaura, Synthesis of nanostructured reduced titanium oxide: crystal structure transformation maintaining nanomorphology, Angew. Chem. 123 (2011) 7556–7559, https://doi.org/10.1002/ange.201101432.

[30] V. Kumaravel, S. Mathew, J. Bartlett, S.C. Pillai, Photocatalytic hydrogen production using metal doped TiO_2: a review of recent advances, Appl. Catal. B Environ. 244 (2019) 1021–1064, https://doi.org/10.1016/j.apcatb.2018.11.080.

[31] N. Rahimi, R.A. Pax, E.M. Gray, Review of functional titanium oxides. I: TiO_2 and its modifications, Prog. Solid. State Ch. 44 (2016) 86–105, https://doi.org/10.1016/j.progsolidstchem.2016.07.002.

[32] J. Cai, J. Shen, X. Zhang, Y.H. Ng, J. Huang, W. Guo, C. Lin, Y. Lai, Light-driven sustainable hydrogen production utilizing TiO_2 nanostructures: a review, Small Methods 3 (2019) 1800184, https://doi.org/10.1002/smtd.201800184.

[33] S.B. Patil, P.S. Basavarajappa, N. Ganganagappa, M.S. Jyothi, A.V. Raghu, K.R. Reddy, Recent advances in non-metals-doped TiO_2 nanostructured photocatalysts for visible-light driven hydrogen production, CO_2 reduction and air purification, Int. J. Hydrog. Energy 44 (2019) 13022–13039, https://doi.org/10.1016/j.ijhydene.2019.03.164.

[34] J.F. Baumard, E. Tani, Electrical conductivity and charge compensation in Nb doped TiO_2 rutile, J. Chem. Phys. 67 (1977) 857–860, https://doi.org/10.1063/1.434952.

[35] J. Arbiol, J. Cerda, G. Dezanneau, A. Cirera, F. Peiro, A. Cornet, J.R. Morante, Effects of Nb doping on the TiO_2 anatase-to-rutile phase transition, J. Appl. Phys. 92 (2002) 853–861, https://doi.org/10.1063/1.1487915.

[36] S. Hussain, H. Erison, N. Kongi, A. Tarre, P. Ritslaid, A. Kikas, V. Kisand, J. Kozlova, J. Aarik, A. Tamm, Platinum sputtered on Nb-doped TiO_2 films prepared by ALD: highly active and durable carbon-free ORR electrocatalyst, J. Electrochem. Soc. 167 (2020) 164505, https://doi.org/10.1149/1945-7111/abcbb4/meta.

[37] T. Potlog, P. Dumitriu, M. Dobromir, A. Manole, D. Luca, Nb-doped TiO_2 thin films for photovoltaic applications, Mater. Des. 15 (2015) 558–563, https://doi.org/10.1016/j.matdes.2015.07.034.

[38] I. Ben Jemaa, F. Chaabouni, L. Presmanes, Y. Thimont, M. Abaab, A. Barnabe, P. Tailhades, Structural, optical and electrical investigations on Nb doped TiO_2 radio-frequency sputtered thin films from a powder target, J. Mater. Sci. Mater. Electron. 27 (2016) 13242–13248, https://doi.org/10.1007/s10854-016-5471-8.

[39] M. Kim, C. Kwon, K. Eom, E. Cho, Electrospun Nb-doped TiO_2 nanofiber support for Pt nanoparticles with high electrocatalytic activity and durability, Sci. Rep. 7 (2017) 44411, https://doi.org/10.1038/srep44411.

[40] C. He, S. Sankarasubramanian, I. Matanovic, P. Atanassov, V. Ramani, Understanding the oxygen reduction reaction activity and oxidative stability of Pt supported on Nb-doped TiO_2, ChemSusChem 12 (2019) 3468–3480, https://doi.org/10.1002/cssc.201900499.

[41] A. Bauer, L. Chevallier, R. Hui, S. Cavaliere, J. Zhang, D. Jones, J. Rozière, Synthesis and characterization of Nb-TiO_2 mesoporous microsphere and nanofiber supported Pt catalysts for high temperature PEM fuel cells, Electrochim. Acta 77 (2012) 1–7, https://doi.org/10.1016/j.electacta.2012.04.028.

[42] L. Chevallier, A. Bauer, S. Cavaliere, R. Hui, J. Rozière, D.J. Jones, Mesoporous nanostructured Nb-doped titanium dioxide microsphere catalyst supports for PEM fuel cell electrodes, ACS Appl. Mater. Interfaces 4 (2012) 1752–1759, https://doi.org/10.1021/am300002j.

[43] S. Hussain, H. Erikson, N. Kongi, A. Tarre, P. Ritslaid, A. Kikas, V. Kisand, J. Kozlova, J. Aarik, A. Tamm, V. Sammelselg, K. Tammeveski, Platinum sputtered on Nb-doped TiO2 films prepared by ALD: highly active and durable carbon-free ORR electrocatalyst, J. Electrochem. Soc. 167 (2020) 164505, https://iopscience.iop.org/article/10.1149/1945-7111/abcbb4.

[44] H. Chhina, S. Campbell, O. Kesler, Ex situ and in situ stability of platinum supported on niobium-doped titania for PEMFCs, J. Electrochem. Soc. 156 (2009) B1232–-B1237https://doi.org/10.1149/1.3184155.

[45] Q. Du, J. Wu, H. Yang, Pt@Nb-TiO_2 catalyst membranes fabricated by electrospinning and atomic layer deposition, ACS Catal. 4 (2014) 144–151, https://doi.org/10.1021/cs400944p.

[46] K.-W. Park, K.-S. Seol, Nb-TiO_2 supported Pt cathode catalyst for polymer electrolyte membrane fuel cells, Electrochem. Commun. 9 (2007) 2256–2260, https://doi.org/10.1016/j.elecom.2007.06.027.

[47] X. Lü, X. Mou, J. Wu, D. Zhang, L. Zhang, F. Huang, F. Xu, S. Huang, Improved-performance dye-sensitized solar cells using Nb-doped TiO_2 electrodes: efficient electron injection and transfer, Adv. Funct. Mater. 20 (2010) 509–515, https://doi.org/10.1002/adfm.200901292.

[48] A. Ohma, K. Shinohara, A. Iiyama, T. Yoshida, A. Daimaru, Membrane and catalyst performance targets for automotive fuel cells by FCCJ membrane, catalyst, MEA WG, ECS Trans. 41 (2011) 775–784https://doi.org/10.1149/1.3635611.

[49] R.D. Shannon, Revised effective ionic radii and systematic studies of interatomic distances in halides and chalcogenides, Acta Cryst A32 (1976) 751–767, https://doi.org/10.1107/S0567739476001551.

[50] R.A. Spurr, H. Myers, Quantitative analysis of anatase-rutile mixtures with an X-ray diffractometer, Anal. Chem. 29 (1957) 760–762, https://doi.org/10.1021/ac60125a006.

[51] D.A.H. Hanaor, C.C. Sorrell, Review of the anatase to rutile phase transformation, J. Mater. Sci. 46 (2011) 855–874, https://doi.org/10.1007/s10853-010-5113-0.

[52] A.M. Ruiz, G. Dezanneau, J. Arbiol, A. Cornet, J.R. Morante, Insights into the structural and chemical modifications of Nb additive on TiO_2 nanoparticles, Chem. Mater. 16 (2004) 862–871, https://doi.org/10.1021/cm0351238.

[53] R.M. Pittman, A.T. Bell, Raman studies of the structure of Nb_2O_5/TiO_2, J. Phys. Chem. 97 (1993) 12178–12185, https://doi.org/10.1021/j100149a013.

[54] R.K. Sharma, M.C. Bhatnagar, Improvement of the oxygen gas sensitivity in doped TiO thick films, Sensors Actuators B Chem. 56 (1999) 215–219, https://doi.org/10.1016/S0925-4005(99)00032-5.

[55] C. Zhang, M. Ikeda, T. Uchikoshi, J.-G. Li, T. Watanabe, T. Ishigaki, High-concentration niobium (V) doping into TiO2 nanoparticles synthesized by thermal plasma processing, J. Mater. Res. 26 (2011) 658–671, https://doi.org/10.1557/jmr.2011.16.

[56] L. Sheppard, T. Bak, J. Nowotny, C.C. Sorrell, S. Kumar, A.R. Gerson, M.C. Barnes, C. Ball, Effect of niobium on the structure of titanium dioxide thin films, Thin Solid Films 510 (2006) 119–124, https://doi.org/10.1016/j.tsf.2005.12.272.

[57] A. Ishihara, M. Arao, M. Matsumoto, T. Tokai, T. Nagai, Y. Kuroda, K. Matsuzawa, H. Imai, S. Mitsushima, K. Ota, Niobium-added titanium oxides powders as non-noble metal cathodes for polymer electrolyte fuel cells–electrochemical evaluation and effect of added amount of niobium, Int. J. Hydrog. Energy 45 (2020) 5438–5448, https://doi.org/10.1016/j.ijhydene.2019.08.217.

[58] K. Monika, V. Galstyan, E. Comini, J. Szuber, Pure and highly Nb-doped titanium dioxide nanotubular arrays: characterization of local surface properties, Nanomaterials 7 (2017) 456, https://doi.org/10.3390/nano7120456.

[59] W. Xie, R. Li, Q. Xu, Enhanced photocatalytic activity of Se-doped TiO_2 under visible light irradiation, Sci. Rep. 8 (2018) 8752, https://doi.org/10.1038/s41598-018-27135-4.

[60] A. Ishihara, J. Hirata, T. Nagai, Y. Kuroda, K. Matsuzawa, A. Imanishi, S. Mitsushima, Y. Takasu, K. Ota, Effect of semiconducting properties of oxide-based compounds on oxygen reduction activity in acidic media, ECS Trans. 98 (2020) 457–464https://doi.org/10.1149/09809.0457ecst.

[61] J. Bisquert, F. Fabregat-Santiago, I. Mora-Seró, G. Garcia-Belmonte, E.M. Barea, E. Palomares, A review of recent results on electrochemical determibation of the density of electronic states of nanostructures metal-oxide semiconductors and organic hole conductors, Inorg. Chim. Acta 361 (2008) 684–698, https://doi.org/10.1016/j.ica.2007.05.032.

[62] K. Kakinuma, K. Suda, R. Kobayashi, T. Tano, C. Arata, I. Amemiya, S. Watanabe, M. Matsumoto, H. Imai, A. Iiyama, M. Uchida, Electronic states and transport phenomena of Pt nanoparticle catalysts supported on Nb-doped SnO_2 for polymer electrolyte fuel cells, ACS Appl. Mater. Interfaces 11 (2019) 34957–34963, https://doi.org/10.1021/acsami.9b11119.